Plasma Sources Science and Technology

Check for updates

PAPER

RECEIVED
16 February 2026

REVISED
29 April 2026

ACCEPTED FOR PUBLICATION
19 May 2026

PUBLISHED
15 June 2026

# Decay of excited levels in argon pulsed capacitively-coupled plasma afterglows

**Lan-Yue Luo[1], Zoltán Donkó[2], Ranna Masheyeva[2], He-Ping Li[1,*] and Peter Hartmann[2,*]**

[1] Department of Engineering Physics, Tsinghua University, Beijing 100084, People's Republic of China
[2] Institute for Solid State Physics and Optics, HUN-REN Wigner Research Centre for Physics,1121 Budapest, Konkoly Thege Miklós str. 29-33, Hungary
[*] Authors to whom any correspondence should be addressed.

**E-mail:** liheping@tsinghua.edu.cn and hartmann.peter@wigner.hu

**Keywords:** pulsed capacitively coupled plasma, afterglow, excited atom kinetics

## Abstract

The decay of excited atom populations is investigated in the afterglow of an argon radio-frequency (RF) capacitively coupled plasma (CCP) experimentally and by means of kinetic simulation of the charged species combined with a fluid description of the excited atoms, including radiative channels. The experiments are conducted in a symmetric CCP, at pressures within the 5–60 Pa range. The Ar $1s_5$ and $1s_3$ metastable atom densities are monitored by tunable diode laser absorption spectroscopy (over a time span of milliseconds) and the intensities of two prominent spectral lines, Ar $2p_1 \rightarrow 1s_2$ (750.39 nm) and $2p_9 \rightarrow 1s_5$ (811.53 nm) are recorded with a conventional optical emission spectroscopy setup (over a time span of tens of microseconds). The discharge simulations allow computation of the spatio-temporal density distributions of the charged species ($e^-$ and $Ar^+$) and of 30 excited Ar levels, including all 1s and 2p levels, in the quasi-steady discharge and in the afterglow plasma, as well as the rates of all elementary processes. Following the termination of the RF excitation, the metastable species exhibit an initial characteristic decay time of the order of 1 ms. At higher pressures, a slower decay is observed on a longer time scale, along with a characteristic change of the spatial distribution of these species. The analysis of light emission reveals that while the excitation mechanism of the $2p_1$ and $2p_9$ levels is different in the active discharge and the early afterglow, at later times, both levels become populated by stepwise electron impact on Ar 1s atoms. The temporal behavior of emission is understood based on the analysis of the populating and depopulating rates of the 2p levels.

## 1. Introduction

Radio-frequency (RF) capacitively coupled plasmas (CCPs) have been widely used for decades in various industrial applications, particularly in the fabrication of microelectronic devices [1]. Among the multiple processes involved prior to chip packaging, CCPs are commonly employed for thin-film deposition [2], doping [3], and are especially important for dry etching [4]. The objectives of plasma etching include achieving high throughput, strong anisotropy, good uniformity, and minimal substrate damage, which necessitates independent control of the ion flux and the ion bombardment energy at the substrate surface. However, in conventional CCPs, these two parameters are inherently coupled, making it difficult to decouple the ion density and energy solely by adjusting the input power [5].

To overcome this problem, various concepts, like dual-frequency excitation [6–8] and the application of tailored voltage waveforms [9, 10], were developed. In addition to these, pulsed plasmas have emerged as promising candidates for overcoming the limitations of conventional continuous-wave (CW) plasmas by introducing additional control parameters, i.e. the pulse frequency and duty cycle [11]. As microelectronic devices continue to shrink, the risk of plasma-induced damage due to surface charging during etching processes becomes increasingly critical. Pulsed plasmas offer a practical approach to achieving etching with less charge build-up damage by injecting negative charges during the power-off period,

© 2026 IOP Publishing Ltd. All rights, including for text and data mining, AI training, and similar technologies, are reserved.

thereby neutralizing the accumulated surface charge on the substrate [12–14]. In addition, pulse modulation of CCPs has been shown to enhance etching uniformity [15]. Understanding the behavior of the power-off period, often referred to as the *afterglow*, is therefore essential for gaining deeper insight into the unique advantages of pulsed plasmas and for improving their performance in practical applications.

It has been well established that long-lived metastable atoms make significant contributions to ionization owing to their low reaction energy thresholds [16, 17]. As long-lived species, metastable levels can store a considerable amount of energy and exert a crucial influence on the dynamics of charged particles. Therefore, it is meaningful to examine the kinetics of excited levels in detail during the afterglow stage. Both experimental and computational studies have been conducted to investigate plasma processes involving metastable levels in the low-pressure afterglow of rare gases. Previous studies have shown that collisions involving metastable atoms can lead to electron re-heating and the appearance of an electron density peak in the early afterglow [18–22]. As the electron energy decreases rapidly due to diffusive cooling [23], excitation and ionization from ground-state (GS) atoms drop sharply. Pooling ionization between two metastable atoms can, however, produce an electron–ion pair, serving as an alternative ionization source. This mechanism can lead to a slight increase in the electron density [18], and the resulting high-energy electrons (around 7 eV for argon) have been observed in the measured electron energy probability function (EEPF) [19]. According to references [20–22], superelastic collisions—in which metastable atoms are de-excited by electron impact—also play an important role in electron heating. Moreover, the fast electrons generated through these processes can enhance the near-wall potential drop, even when their density is much lower than that of the bulk electrons [24]. Similar heating effects associated with metastable atoms have also been reported in studies of the electron energy evolution in inductively coupled plasmas (ICPs) [25], although in some cases the effect originates from recombination processes under high electron densities [26, 27]. Simulations considering recombination processes were also conducted for low-pressure CCPs [28]. However, the excited levels were not included in this model.

In addition to metastable levels, higher excited levels also play a significant role in low-pressure discharges. As the electron temperature decreases rapidly in the afterglow, excitation from GS atoms to higher excited levels becomes negligible, leaving the metastable levels as the dominant excitation source [29]. Consequently, the light emission from the higher excited levels can be used to determine specific rate coefficients of the stepwise excitation by electron impact [30, 31], as well as the effective electron temperature [32].

The temporal evolution of excited levels during the afterglow, particularly that of metastable levels, has attracted considerable interest. A global collisional-radiative model (CRM) was employed to investigate metastable densities in pure argon afterglow plasmas [33]. The calculated results showed good qualitative agreement with laser absorption measurements and revealed that, among the loss processes, electron collisions dominate initially, followed by diffusion as the major loss mechanism. A more advanced CRM combined with a particle-in-cell/Monte Carlo collision (PIC/MCC) model was later used to study the temporal dynamics of argon metastable and resonant levels in CCP afterglows [22]. These studies confirm that depopulation by electron impact and diffusion are the primary loss channels for both metastable levels during the early afterglow of low-pressure Ar CCPs. The situation could be quite different for low-pressure ICPs, where the metastable density rises later as indicated in [34].

As described above, it is meaningful to deepen the understanding of dynamics of excited levels during the afterglow, when no external power is supplied. In this work, a hybrid model combining a one-dimensional PIC/MCC code with a one-dimensional diffusion–reaction–radiation (DRR) code is employed to investigate the temporal dynamics of argon excited levels. The present model is an extension of our previous version, which was used to calculate absolute metastable densities in CW CCPs and showed good agreement with experimental measurements [35]. The DRR model is essentially a CRM, which also includes the spatial transport of the excited species. Following [36], we consider 30 Ar-I excited levels in our calculations. To our best knowledge, no such detailed investigation of the excited levels kinetics in argon afterglows exists in the literature. Time-resolved optical emission spectroscopy (OES) and tunable diode laser absorption spectroscopy (TDLAS) are used to validate the simulation results during the afterglow period. With the TDLAS, we measure the time-dependent densities of the Ar $1s_5$ and $1s_3$ metastable atoms at the center of the electrode gap, while the OES provides the time-dependent emission intensities from the discharge center on the Ar-I 750.39 nm and 811.53 nm transitions, originating from the $2p_1$ and $2p_9$ levels, respectively.

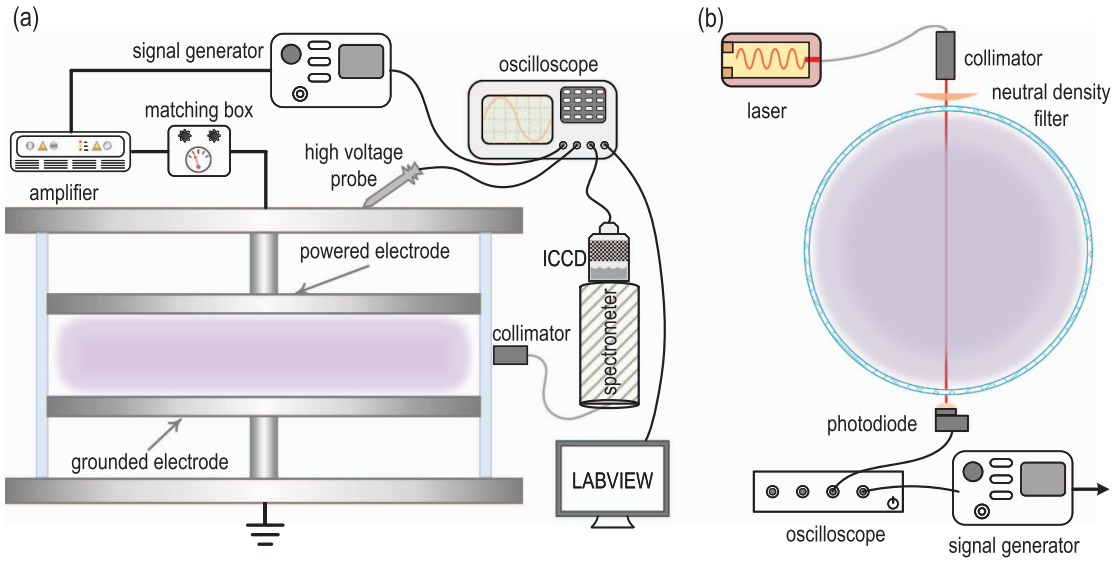



**Figure 1.** Schematic of experimental setup showing the discharge chamber from the side (a) and from the top (b).

The combined use of simulation and experiment provides deeper insight into the temporal behavior of plasmas within the studied pressure regime. The structure of this paper is as follows: section 2 introduces the experimental setup and diagnostic techniques; section 3 describes the simulation model and parameters; section 4 provides a brief discussion of the error and accuracy analysis. The results and discussions are presented in section 5, followed by the conclusions in section 6.

## 2. Experimental setup and methods

The schematic of the experimental configuration is presented in figure 1. The discharge chamber is a geometrically symmetric reactor ('Budapest v.3' cell) equipped with parallel electrodes, made of 304-type stainless steel with equal diameters of 14 cm and positioned at a separation of 4 cm, situated within a quartz (fused silica) cylinder. As metastable Ar atoms are particularly susceptible to quenching by molecular impurities, care has to be taken to achieve sufficiently clean and well-defined conditions for our experimental investigations. Argon gas with a purity of 6.0 is introduced into the system via the cryotrap, which is maintained within the temperature range of $-80^{\circ}$ C to $-50^{\circ}$ C, using a chilled ethanol bath. This process is intended to trap any residual water impurity that can be present in the feed gas at the ppm level. The experiments are conducted in a flowing gas environment, where the gas flow is maintained at a constant rate of 1 sccm by a mass flow controller. The gas pressure is varied from 5 Pa to 60 Pa by adjusting a needle valve at the pump side of the chamber. The ultimate gas impurity concentration can be estimated by comparing the gas flow rate to the 'leak rate' of the system with closed input and output valves, which has been measured to be $1.2 \times 10^{-5}$ sccm. This leak rate includes both the degassing of the internal surfaces and the leakage due to unavoidable imperfections of vacuum fittings.

The spectral measurements provide further evidence of the high gas purity of the discharge. Spectroscopic analysis of the plasma emission in the wavelength range between 250 nm and 900 nm results in the identification of all spectral features, as shown in figure 2 for an active CCP discharge at 20 Pa. The OH emission band is hardly visible just above 300 nm wavelength, the rest of the features have been identified as Ar-I or Ar-II transitions. No discernible emission bands of oxygen or nitrogen molecules can be found.

The pulsed RF signal, appropriate for the OES investigation of the afterglow, is constructed using a dual-channel signal generator (BK Precision 4046B), capable of producing phase-locked amplitude modulation of the 13.56 MHz sinusoidal wave with a 13.56 kHz (50% duty cycle) square signal, resulting in repeated 36.87 $\mu$s (500 cycles) RF on and 36.87 $\mu$s RF off phases. The pulsed RF signal is amplified by a broadband RF power amplifier (Vectawave VBA100-200) and fed to the powered (top) electrode through a manual impedance matching unit (Tokyo HY-power MB-300). The electrode voltage is measured using a high-voltage probe (Tektronix P5100A) connected to an oscilloscope (Tektronix MSO44), which is triggered by the low-frequency square signal output of the signal generator. The resulting RF voltage is

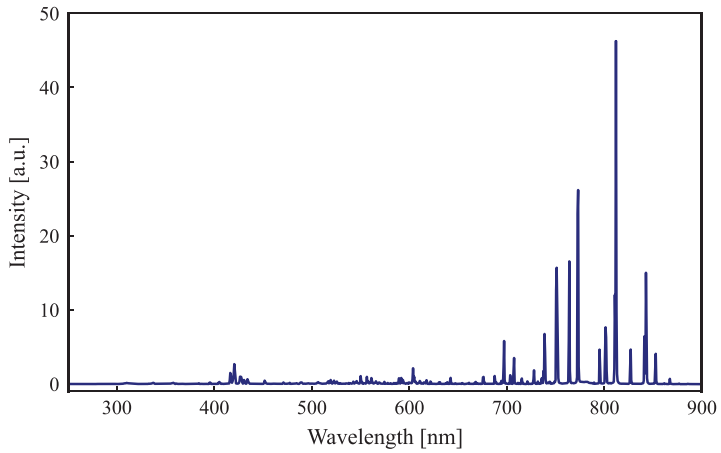



**Figure 2.** Optical emission spectrum of the active CCP discharge at 20 Pa.

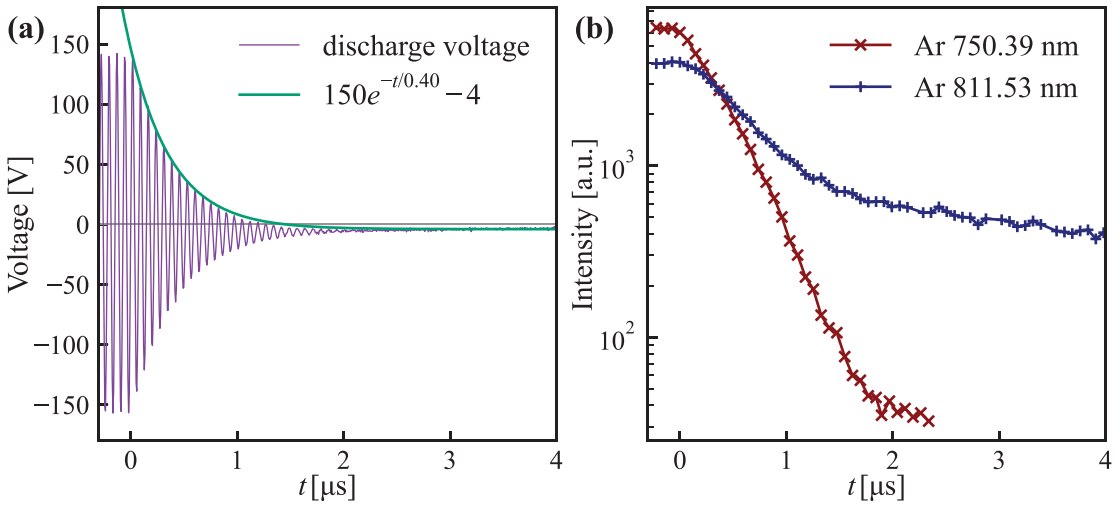



**Figure 3.** (a) Falling edge of the pulsed RF driving voltage with an exponential fitting and (b) light emission at 750.39 nm and 811.53 nm, measured at 5 Pa. The data in (a) show the presence of a small DC self-bias voltage of −4 V, which is marginal in comparison with the voltage amplitude of 150 V, due to the highly symmetric plasma source configuration.

characterized by a steady 150 V amplitude during the power-on phase, followed by an exponential decay of the RF amplitude to zero over 1.8 $\mu$s, followed by a 35 $\mu$s period at 0 V. The measured 150 V→0 V transient is illustrated in figure 3(a). The exponential decay of driving RF voltage causes an instant drop in both light emission signals that we investigate, as illustrated in figure 3(b), but on obviously different orders of magnitude (analyzed later).

For OES, a spectrometer (Carl-Zeiss Jena PGS-2, with 2 m focal length and a spectral resolving power of 45 600) equipped with a fast gated intensified CCD camera (4 QuickE, Stanford Computer Optics) is employed. Line-integrated emission from the central region of the discharge is fed into the spectrometer via a fiber collimator (Thorlabs F220SMA-A) and an optical fiber (Thorlabs M92L02). The light emission from the Ar $2p_1 \rightarrow 1s_2$ and $2p_9 \rightarrow 1s_5$ transitions is measured, at wavelengths of 750.39 nm and 811.53 nm, respectively. The first of these transitions is known to be preferentially excited by fast electrons from ground state atoms, while the second is sensitive to stepwise excitation from the Ar $1s_5$ metastable level [37]. The ICCD camera is triggered by the low-frequency square modulation signal of the signal generator, using a constant gate time of 73.75 ns (one RF cycle) and at delay times increasing by the same amount, scanning the afterglow period until the light intensity reaches the lower detection limit. The exposure time of the CCD is set to 10 s and 60 s, resulting in the integration of light from about 135 000 and 810 000 modulation cycles for the early and late afterglow times, respectively.

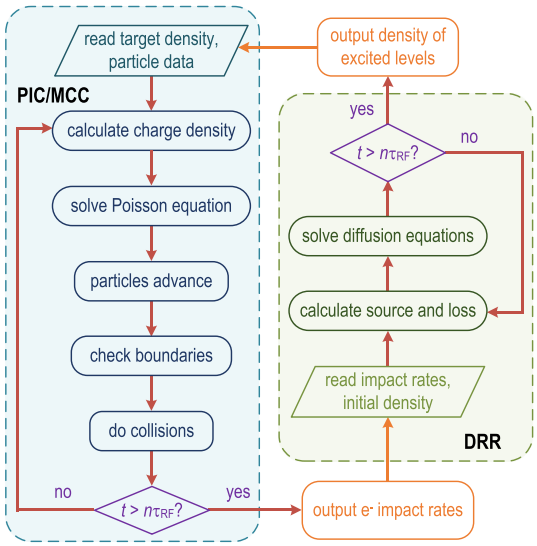



**Figure 4.** Flow chart of the numerical code.

In the TDLAS measurements, the light of a single-mode diode laser (Toptica LD-0773-0075-DFB-1) is fed through the discharge cell along its diameter, at a position corresponding to the center of the electrode gap, and is detected by a photodiode (Thorlabs APD130A2/M), as shown in figure 1(b). For the quasi-steady CW CCPs, the laser wavelength is periodically modulated in time, as done in our previous work [35], to scan the entire absorption line, and the absolute metastable density is calculated based on the area under the absorption profile after background removal. However, in order to obtain a high temporal resolution in the afterglow of interest here, the laser wavelength is fixed at the peak of the absorption profile, and the time evolution of the absorption is measured to obtain the line-of-sight integrated metastable atom density. The frequency of the square wave modulation signal is reduced to 67.8 Hz for the TDLAS measurements, providing power on and off periods with 7374 $\mu$s duration each.

## 3. Simulation model

The simulations employ a hybrid framework combining a PIC/MCC module with a DRR code to model the discharge. The former tracks macro-particles representing electrons and argon ions, resolved in one spatial dimension and three velocity components (1d3v). The latter solves the rate equations for the one-dimensional density distributions of 30 argon excited levels based on a fluid approach. A similar hybrid approach has previously been applied to compute metastable argon atom densities in CCPs sustained in pure argon [17] and argon/oxygen mixtures [35].

In the earlier implementation reported in [35], a unidirectional coupling from the PIC/MCC module to the DRR (fluid) module was adopted to reduce the computational cost for gas mixtures. However, this data flow limited the applicability of the model to quasi-steady discharges at low pressures ($<$10 Pa), where the EEPF is only weakly affected by the presence of populations in excited levels [17].

In the present work, the temporal evolution of excited-level populations during the afterglow period is investigated. In the PIC/MCC module, the excited species are treated as background fluids defined by their density profiles, while the electron-impact reaction rates involving these levels are exported as source or loss terms for the DRR solver. The densities of the excited levels are updated every few RF cycles, with the period of a single RF cycle being $\tau_{RF} \approx 0.07\,\mu$s. A schematic of the main processes in the numerical workflow is shown in figure 4. This numerical scheme has substantial computational demands, resulting in long simulation runtime, of typically 2 weeks on a single Intel Xeon Gold 5320 H CPU.

### 3.1. The PIC/MCC code

The 1d3v PIC/MCC code, named *PICit!*, includes a classical electrostatic field solver and employs the null-collision method. It has been successfully applied to studies of CCPs in rare gases and gas mixtures, with results verified against experimental data [38–40]. In the simulation, electrons and ions are

**Table 1.** Particle processes considered in PIC/MCC code. Ar* denotes various excited levels of argon atoms.

| Reaction | Process | Reference |
|---|---|---|
| $e^- + Ar \rightarrow e^- + Ar$ | Elastic scattering | [42] |
| $e^- + Ar \rightarrow e^- + Ar^*$ | Excitation (to 31 levels) | [42] |
| $e^- + Ar^* \rightarrow e^- + Ar^{**}$ | Excitation to higher levels | [42] |
| $e^- + Ar^{**} \rightarrow e^- + Ar^*$ | De-excitation to lower levels | [42] |
| $e^- + Ar^* \rightarrow e^- + Ar$ | De-excitation to GS | [42] |
| $e^- + Ar \rightarrow 2e^- + Ar^+$ | Direct ionization | [42] |
| $e^- + Ar^* \rightarrow 2e^- + Ar^+$ | Stepwise ionization | [47] |
| $Ar^* + Ar^* \rightarrow e^- + Ar^+ + Ar$ | Pooling ionization | [48] |
| $Ar^+ + Ar \rightarrow Ar^+ + Ar$ | Elastic scattering (isotropic + backward) | [49] |

represented as macro-particles (typically $\sim 10^5$), while neutral species are treated as a stationary background for collisions. The GS atom density is assumed to be uniformly distributed between the electrodes, calculated from the gas pressure. The densities of Ar atoms in the metastable levels ($1s_5$ and $1s_3$) are typically several orders of magnitude lower than that of the GS atoms, and are imported from the results of the DRR code. The density distributions of the atoms in the other excited levels are also taken from the DRR calculations, with values that are typically several orders of magnitude lower than those of metastable levels.

The simulation domain is divided into 512 cells, and the number of time steps within one RF cycle ranges from 4000 to 12 000, depending on the pressure. The setting of grid division and time steps ensures the stability criterion for quasi-steady discharge during the power-on period, including resolution of the Debye length and electron oscillation. Besides, the collision probabilities in a single time step for both electrons and ions are smaller than 0.05 to minimize the possibility of multiple collisions. The number of macro-particles for either electrons or ions ranges from $1 \times 10^5$ to $2 \times 10^5$, ensuring more than 100 particles per cell. For secondary electron emission at the boundaries, the effective yield for argon ion bombardment is taken to be $\gamma = 0.07$, while the effective reflection coefficient for electrons is set to $r = 0.7$ based on the findings in [41].

The collision processes between charged particles and neutral targets include elastic scattering, excitation, de-excitation, and ionization. Electron impact excitation from GS atoms considers 31 excited levels, including Rydberg levels. In addition, stepwise excitation processes between excited levels are incorporated. The cross sections from the BSR dataset [42, 43] of LXCat [44, 45] are used. The de-excitation cross sections are derived from the principle of detailed balance, following [46]. The ionization model for electrons includes both direct ionization from the ground state and stepwise ionization from the 1s and 2p levels. The cross sections for stepwise ionization processes are assumed to be identical for all 1s levels, and are taken from [47]; the same assumption is applied to the 2p levels. Furthermore, pooling ionization involving the 1s levels contributes to the generation of charged particles, with rate coefficients adopted from [48]. For ions, only elastic scattering processes with GS atoms are taken into account [49]. A summary of all collision processes considered is provided in table 1.

For PIC/MCC modeling, the number of macro-particles is known to have some effects on the accuracy of the calculated macroscopic quantities, such as charged particle densities and collision rates [50, 51]. A sufficiently large number of macro-particles is required to obtain stable and physically reliable statistics. However, during the afterglow, the densities of charged particles gradually decrease due to losses at the electrodes, resulting in a reduction in the total macro-particle number. To compensate for this effect, adaptive particle management [52] is introduced to maintain the number of macro-particles. Specifically, randomly selected macro-particles are split into two, each assigned half of the original weight, so that the number of macro-particles remains approximately constant over the course of the afterglow, when the plasma density decays. The number of macro-particles to be split is determined based on the particle losses observed over the preceding several RF cycles.

### 3.2. The DRR code

The density distributions of excited Ar atoms are updated in the DRR code after certain RF cycles simulated with the PIC/MCC module, which yields the time-averaged spatially-resolved electron impact rates involving population and de-population of 31 excited levels. The excitation rates from GS atoms to Rydberg levels are included due to their importance as a cascade source contributing to the 1s levels. It should be noted that the RF cycle is not temporally resolved in the DRR calculation. Instead, the

electron impact rates are used as self-consistent source terms over several RF cycles in the DRR code. Therefore, the results of the DRR model focus on the evolution on timescales several times of the RF period, rather than the instantaneous RF-resolved dynamics.

Similar to our previous model, the rate equations are different for long- and short-time levels [35]. For argon atoms above the 1s levels, diffusion is excluded. Therefore, the source and loss terms for levels above the 2p levels come from the electron impact and radiation, expressed as:

$$\frac{\partial n_k}{\partial t} = S_{\mathrm{EI}}(x,t) + S_{\mathrm{RAD}}(x,t). \tag{1}$$

Additional quenching by GS atoms is included for the 2p levels, with coefficients taken from [53, 54]:

$$\frac{\partial n_k}{\partial t} = S_{\mathrm{EI}}(x,t) + S_{\mathrm{RAD}}(x,t) - k_{\mathrm{Q}} n_k n_{\mathrm{Ar}}. \tag{2}$$

The source and loss channels are more complex for the 1s levels. Compared with the 2p levels, additional processes are taken into consideration, including axial and radial diffusion, cascade from Rydberg levels and pooling ionization, expressed as:

$$\frac{\partial n_k}{\partial t} = \frac{\partial}{\partial x}\left(D\frac{\partial n_k}{\partial x}\right) - \nu n_k + S_{\mathrm{EI}}(x,t) + S_{\mathrm{RAD}}(x,t) + S_{\mathrm{CAS}}(x,t) - k_{\mathrm{Q}} n_k n_{\mathrm{Ar}} - k_{\mathrm{P}} n_k n_{1\mathrm{s}}. \tag{3}$$

For the (reduced) diffusion coefficient, we adopt the value $D \cdot N = 1.7\times10^{20}(\mathrm{m\cdot s})^{-1}$ from [55], where $N$ is the number density of GS atoms. We apply the Robin boundary condition with the reflection coefficient $\gamma_{\mathrm{r}} = 0.5$ adopted from [16] for the solution of the above balance equations. Radial diffusion is calculated with the characteristic frequency $\nu = D/(R/2.405)^2$, where $R$ is the radius of the electrode. The influence of Rydberg levels is incorporated by distributing their excitation rates to four 1s levels. The distribution ratio is based on the radiation rates from 2p levels to each 1s level. The quenching rate constants for 1s atoms by collisions with GS atoms are given in [56].

After the accumulation of sources and losses, the above equations are solved numerically employing an explicit, finite difference, forward-time-centered-space procedure [16]. The numerical configuration is based on 60 grid points and a time interval of $10^{-10}$ s, satisfying the von Neumann stability boundary condition for diffusion equations [57].

The radiative loss of the excited level $k$, radiating to another level $m$, $S_{\mathrm{RAD}}^{(k\to m)}(x,t)$ is computed as

$$S_{\mathrm{RAD}}^{(k\to m)} = -n_k A_{k,m} \eta_{k,m}, \tag{4}$$

where $A_{k,m}$ and $\eta_{k,m}$ are, respectively, the Einstein coefficient and the escape factor of the given transition. The former is taken from [58], while the functional form of the latter is adopted from [59, 60]. The escape factor expresses the strength of the re-absorption of the radiation in the presence of an appreciable density of absorber atoms. For the resonant transitions this effect is very strong as ground state atoms act as absorbers; nonetheless resonant radiation is one of the important pathways of the 'outflow of energy' from the plasma. Due to the appreciable densities of Ar atoms in the 1s levels, the 2p→1s transitions are also partially reabsorbed, i.e. $0.1 < \eta_{k,m} < 1$ for these transitions as well, and this effect cannot be neglected. The intensities of the spectral lines radiated by the plasma, which will also be compared with experimental data, are calculated as $I_{\mathrm{RAD}}^{(k\to m)} = |S_{\mathrm{RAD}}^{(k\to m)}|$.

### 3.3. Coupling of two modules

Although the coupling between the PIC/MCC and DRR modules has been briefly mentioned above, the practical implementation is summarized here for clarity. Typically, after a few RF cycles (which is 2 during the pulse falling edge and 10 for other conditions) of the PIC/MCC simulation, the time-averaged and spatially resolved electron-impact rates over this period are exported to the DRR code. The time average suppresses the statistical noise while providing sufficient temporal evolution for simulation results. The DRR code is then executed over the same time span to compute the evolution of the density distributions of the excited levels, which are subsequently imported into the next PIC/MCC run.

For the afterglow simulations, a preceding power-on phase is required. Initially, the two modules are executed alternately until the densities of metastable levels and charged particles converge under the specified discharge conditions. After convergence is achieved, the external RF voltage is switched off over a short transient period of about 2 $\mu$s, exactly as in the experiment. The PIC/MCC and DRR modules then continue to operate alternately throughout the power-off stage. This simulation approach closely mimics the experimental scenario. Although the discharge is repetitively pulsed in the experiment, the

duration of the plasma-off period is expected to influence only the breakdown process of the next pulse and the charged particle and Ar excited-level populations, provided that the pulse-on period is long enough, just like in our case. Therefore, this re-ignition process is not covered in the simulations for efficiency.

## 4. Notes on errors and accuracy

Below, we give a brief and approximate analysis of possible errors in the experimental and computational results. Regarding the experimental system, sources of errors, their estimates, and our strategies to minimize these are as follows:

- The presence of trace amounts of impurities in the feed gas: as explained above, contamination is minimized by using a high purity (6.0) gas supply, a cryogenic trap, flowing gas and we have regularly confirmed the low leakage rate of the setup;
- The error of pressure measurement: according to the manufacturer, the error of pressure reading is 0.2%, but no less than 0.2 Pa due to the shift in time of the zero pressure reference point;
- The error of voltage measurement: the errors originating from the limited accuracy of the high-voltage probe and the reading by the oscilloscope should not exceed 5%. Another component for the uncertainty of the voltage measurement originates from the fact that the actual RF voltage between the electrodes may differ from the value measured outside the discharge cell (although close to the powered electrode) [61]. For our system, this results in an uncertainty of the level of up to 10%;
- Finite dynamic range of the detectors in the optical measurements: saturation is avoided in all measurements. This error is estimated to be less than 10%; an additional uncertainty arises from the dark signal level of the CCD, which is operated with long exposure times (10 to 60 s), resulting in significant and fluctuating dark signals that need to be subtracted from the raw data. The standard deviation of the dark signal (based on multiple recordings) can be quantified in absolute intensity values rather than percentages, and is different for each combination of the fast gate time and the slow CCD exposure time, which is the reason behind the variation of the error-bar magnitudes in figure 11.
- Data evaluation in the metastable atom density measurements: the Gaussian absorption profile fitting procedure shows a reproducibility for the absolute value of the metastable atom density within 15%; the fast temporal decay measurement is, however, a relative measurement, building on the assumption that the width of the absorption profile (and thus the neutral gas temperature) is constant, and shows a reproducibility within 5%; it is important to emphasize that the TDLAS measurement represent a line-of-sight averaged metastable density value along the diagonal of the cylindrical discharge, which can be significantly lower than the values at the discharge axis, depending on the radial distribution, which, on the other hand, depends on discharge parameters, such as gas pressure and voltage amplitude.

Among all of these, the uncertainty of the RF voltage measurements is believed to be the dominant factor. The charged particle densities are expected to have the same order of uncertainty if a nearly linear connection between the voltage and these densities is assumed, as found in [5] for similar conditions. A similar uncertainty can also be assumed for the excited level densities. The reproducibility of the measured data is found to be well acceptable, within a range of 15%. Considering all the contributions above, the error in the measurement of the 1s level populations is estimated to be about 20%.

For the computational model and its input data, the possible sources of errors are:

- A one-dimensional model and numerical code is used, which cannot account for radial particle losses (except for effective diffusion losses) and radial variations of the charged particles' and excited atoms' density profiles. For the profiles, we contemplate a decaying trend towards the discharge cell wall;
- Escape factors are used to account for the trapping of radiation, which is indeed an approximate way of treating this effect;
- Although the set of elementary processes considered in the model is believed to be fairly complete, at the highest pressures, formation of molecular ions and excimer molecules might start playing some role [62];

- Electron-impact collisions are described with a consistent cross section set that originates from a single source [42, 43], however, the accuracy of some of the cross sections (actually those controlling the population redistribution among the Ar 1s levels) was already questioned in a previous study [63].

Exact error estimation for the first point would require two-dimensional simulations, which are being developed and will be reported in future publications. In the absence of such 'reference results' only a rough estimation, based on the aspect ratio of the electrode gap can be given. With the diameter to gap ratio of $\approx 14/4$, the charged particle fluxes at the plasma source envelope can be estimated to be at least an order of magnitude smaller than the fluxes at the electrodes, due to the fact that the former is controlled by a weak ambipolar field and the latter by the strong sheath electric field. As to the radial dependence of the excited atom densities, in an experiment using a GEC reference cell [64], actually an increase of the metastable $1s_5$ atom density with increasing distance from the cell axis was found for similar discharge conditions as used by us. The measured data in this work seem to extend outside the electrode edges, suggesting that the plasma was not confined to be within the volume defined by the electrodes (typical for GEC cells). Therefore, a direct comparison between the results of [64] and the present data is not possible. The two-dimensional fluid calculations presented in [48] showed a relatively flat density profile for the argon metastable atoms within the region defined by the electrodes that decayed rapidly at the electrode edges and further in the volume outside the electrodes. An increase in $1s_5$ atom density from the discharge axis towards the electrode edges was also found in computerized tomography studies of a dual-frequency CCP in [65]. The geometry considered in this work, however, also included a large additional volume outside of the perimeter of the two powered electrodes, similarly to [48], i.e. no absorbing boundaries at the electrode edges were present in either of the three studies mentioned here, in sharp contrast with the setup used in our work. Therefore, we trust that a radially decreasing density profile does exist in our experimental system, and therefore the simulations are expected to overestimate the radially averaged experimental densities. In the extreme case of a linearly decreasing profile with zero value at the boundary, a factor of two would be expected between the measured and calculated data, however, a significantly weaker decay is expected in reality also because of the reflection of the metastable atoms at the wall.

## 5. Results and discussions

Below, we present computational results for the time-dependent dynamics of the Ar 1s and 2p levels and other discharge characteristics. Simulations and experiments are conducted with an initial voltage amplitude of 150 V, over the pressure range of 5-60 Pa, with a discharge gap of 4 cm. For two metastable levels ($1s_5$ and $1s_3$) and two selected 2p levels ($2p_1$ and $2p_9$) experimental data—obtained, respectively, from laser absorption measurements and OES—are also presented.

Because each excited level is governed by distinct population and depopulation channels, their density evolution during the afterglow exhibits characteristic differences. Therefore, the results are presented in two separate subsections, focusing on the metastable levels and the higher excited levels, respectively.

### 5.1. Metastable levels

As the evolution of the density distributions in the afterglow phase starts from quasi-steady conditions both in the experiments and in the computations, a comparison of the absolute density values obtained for the quasi-steady stage by both approaches is important to validate the computational model. Figure 5 presents this comparison. Overall, a good agreement is observed over the whole pressure range investigated. Quantitatively, the ratios of the computed densities to the experimentally measured values lie between 1.12 and 1.75. The systematic deviation can be explained by the fact that the numerical model is one-dimensional and therefore it cannot account for any radial variation of the excited atom densities present in the experiment. As these densities are expected to decay towards the envelope of the discharge cell, the (averaged) densities measured in the experiment are expected to be lower as compared to the densities at the cell axis.

Turning now to the temporal evolution of Ar $1s_5$ density, the computational results under different pressures are shown with spatial distribution in figure 6. Time point $t = 0$ is the moment of RF power cut-off. The density distributions are symmetric owing to the symmetric configuration of the system. The initial density profile exhibits a clear pressure dependence: it transitions from a concave profile at lower pressures (due to non-local excitation by high energy electrons) to a saddle-shaped structure at higher pressures. This behavior is consistent with previous observations [17, 66]. The emergence of two density maxima with increasing pressure near the electrodes originates from electron-impact excitation

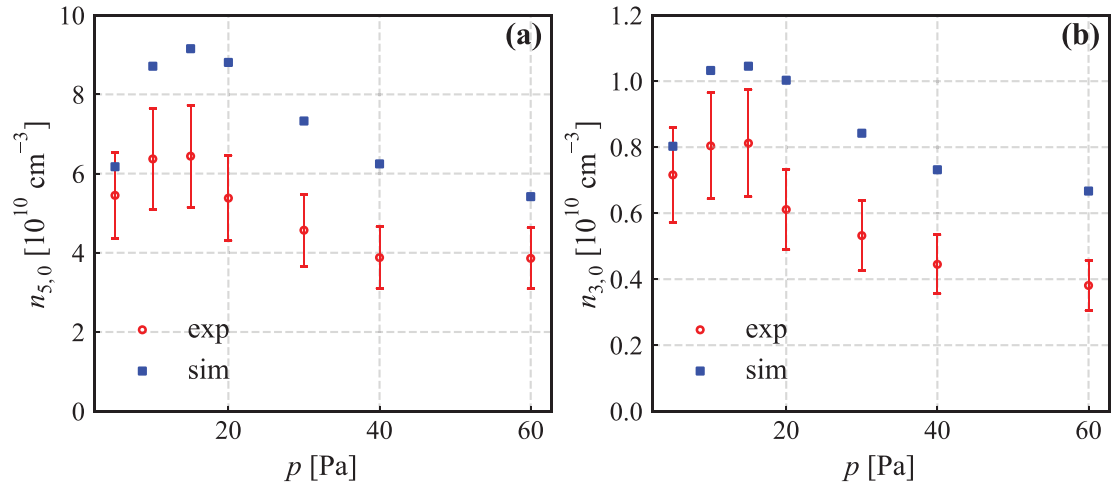



**Figure 5.** Experimentally measured and computed densities of $1s_5$ (a) and $1s_3$ (b) atoms at the mid-plane of the discharge, in the quasi-steady state (at $t \leqslant 0$) under different pressures.

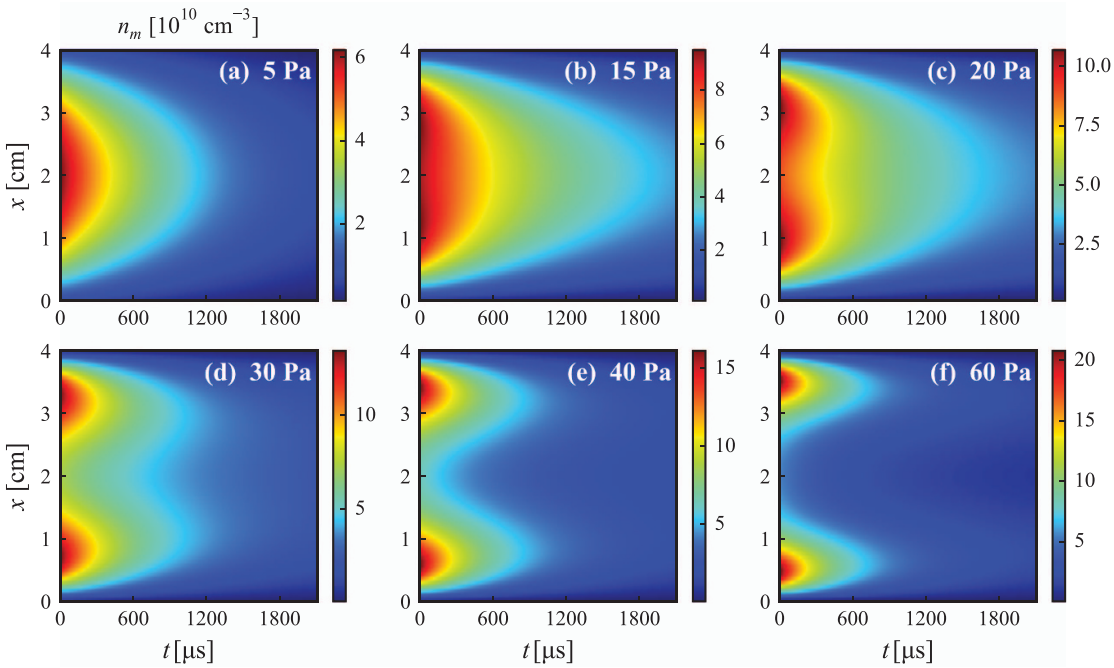



**Figure 6.** Computed spatio-temporal evolution of Ar $1s_5$ density during the afterglow under different pressures.

of GS atoms, which takes a pivotal role in the population of excited levels. As the pressure increases, this process becomes more local and follows gradually more the energy gain of the electrons upon sheath expansion.

Within the parameter range considered here, the profile transition occurs at the pressure of approximately 15 Pa. At lower pressures, the initially centered density peak is retained and a swift overall reduction in density is observed. In contrast, at higher pressures, the temporal evolution is obviously influenced by the saddle-shaped initial distribution. Owing to the pronounced initial gradients, the density exhibits a clear smoothing behavior: the two maxima near the electrodes gradually diminish, while the central region—initially a density minimum—evolves into a dominant peak. This redistribution proceeds in a manner that reflects the diffusion from both sides toward the center. At 20 Pa, this behavior is particularly evident, demonstrating the progressive transformation from a double-peaked profile to a single, centrally concentrated density maximum. At the highest pressure considered, the double-peaked spatial distribution of the Ar $1s_5$ atoms is retained due to suppressed diffusion.

The temporal evolution of the density profile of Ar $1s_3$ atoms closely follows the pattern of $1s_5$ atoms, and is therefore not shown here. The other two 1s levels, the resonant $1s_4$ and $1s_2$, exhibit a

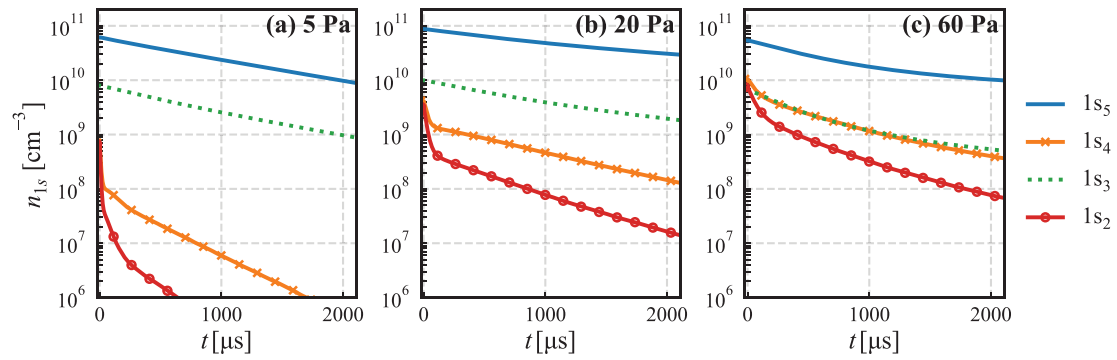



**Figure 7.** Temporal evolution of central densities of Ar atoms in the 1s levels at different pressures, as obtained from the simulations.

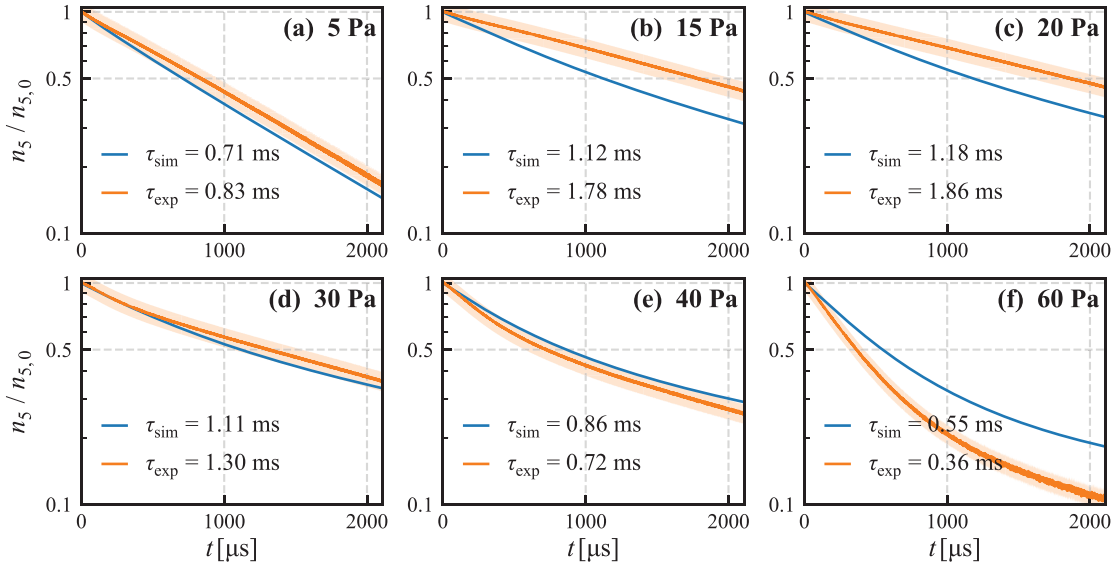



**Figure 8.** Temporal evolution of the Ar 1s$_5$ density normalized by its initial value $n_{5,0}$ under different pressures. Here $\tau$ represents the time when the density decreases to half of its initial value. The shaded areas represent the uncertainty in the experimental data.

much faster temporal decay than the metastable atoms at the low pressure of 5 Pa, as figure 7(a) illustrates. The decay of the population in the 1s$_2$ level is particularly fast, presumably because of the much higher Einstein coefficient of $A(1s_2 \rightarrow \mathrm{GS}) = 5.1 \times 10^8\ \mathrm{s}^{-1}$, as compared to the value $A(1s_4 \rightarrow \mathrm{GS}) = 1.19 \times 10^8\ \mathrm{s}^{-1}$ [67]. The temporal decay of these resonant excited levels slows down with increasing pressure (see figures 7(b) and (c)), due to the enhanced radiation trapping, as indicated by the decrease in the escape factors from $10^{-4}$ under 5 Pa to $10^{-5}$ under 60 Pa. In addition, reduced diffusion losses and enhanced collisional coupling among the 1s levels through collisions with slow electrons may also contribute to the slower decay.

A quantitative comparison of the Ar 1s$_5$ density decay at the discharge center, obtained experimentally and in the simulations is presented in figure 8. The data are plotted in a normalized form, with respect to the values at the beginning of the afterglow, $t = 0$. Owing to the non-exponential decay of the metastable population, especially at elevated pressures, a single effective decay constant cannot adequately describe the afterglow dynamics. Therefore, the decay rate is characterized by the time $\tau$, required for the normalized density to decrease to half of its initial value. The extracted characteristic decay times show reasonable agreement between simulations and experiments. As the gas pressure increases, the decay rate first decreases and then increases, exhibiting a non-monotonic pressure dependence that is consistently observed in both the simulation and experimental results.

Despite the reasonable agreement in the decay trend, the discrepancy between experiment and simulation reveals a pressure-dependent mismatch in the decay rates of the metastable atom density. At low pressures, the computed decay is slightly faster than the experimental one, while at high pressures, the

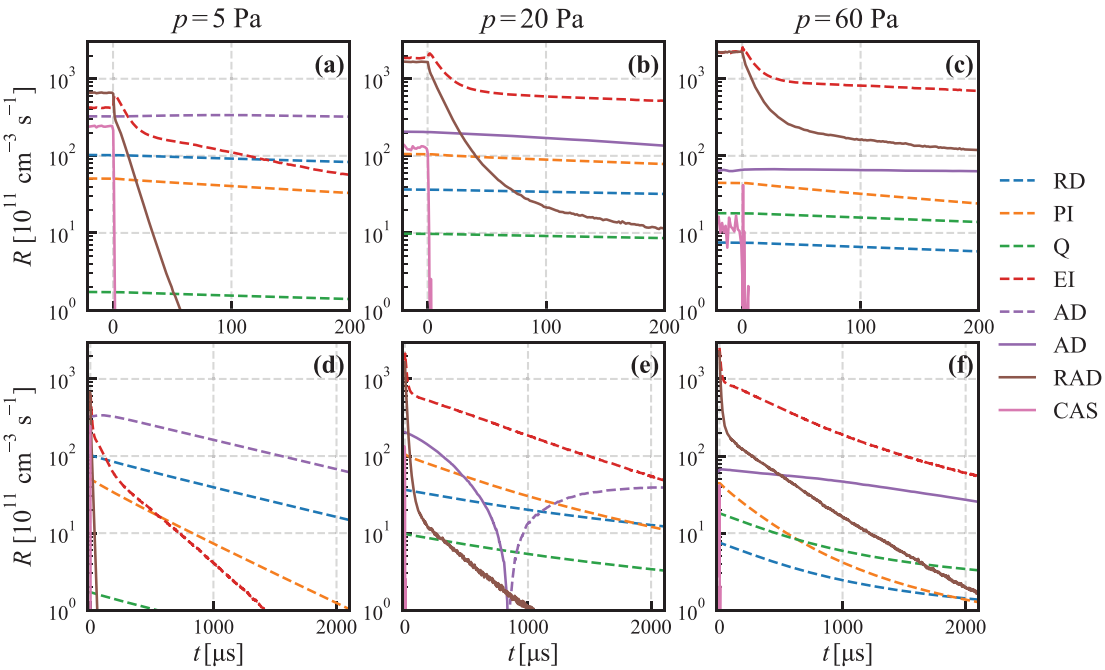



**Figure 9.** Temporal evolution of the Ar $1s_5$ related process rates at the center of the discharge for pressures of (a) 5 Pa, (b) 20 Pa, and (c) 60 Pa, during the first 200 $\mu$s in the afterglow. Panels in the bottom row (d), (e), (f) display the rates over an extended timescale. The dashed lines represent losses and solid lines the sources. 'RD', 'PI', 'Q', 'EI', 'AD' denote radial diffusion, pooling ionization, quenching by neutrals, net electron impact and axial diffusion; 'RAD' and 'CAS' denote population from radiation and cascade sources.

experimental decay becomes faster than the computed one. This crossover behavior could result from overestimated radiation trapping in the simulations. The metastable density along the central axis is larger than that of other radial locations in the experimental discharge chamber. Such higher densities of these levels result in a lower probability of photon escape, which will slow down the decay of 2p levels. Since radiation is one of the important sources during the afterglow period (as it will be shown later), the slow decay of 2p levels will extend the lifetime of metastable levels to some extent, resulting in the slower decay in simulations compared to that in experiments shown in figure 8(f).

At pressures below 20 Pa, the central metastable density decays almost exponentially for a long period. For higher pressures, the exponential decay can be divided into two stages: a fast decay for initial hundreds of microseconds and a slower decay in the later afterglow. The difference in the characteristics of the decay under different pressures can be clarified by analyzing the rates of the population and depopulation processes of the $1s_5$ level at the center of the electrode gap, as illustrated in figure 9.

Under low-pressure conditions, electron-impact stepwise excitation ('EI', at earlier times) and diffusion ('AD', at later times) serve as the dominant loss mechanisms, see figure 9(a) and (d). It is noteworthy that, as the data are presented using a logarithmic scale for the rates, negative values cannot be shown and therefore two curves are shown for axial diffusion: a solid curve for the source and a dashed curve for the loss, respectively. The diffusion term is strongly influenced by the pressure-dependent evolution of the metastable density distribution. Under higher pressures, the metastable density exhibits a central minimum at the beginning of the afterglow (as seen in figure 6), so diffusion initially acts at the discharge center as a secondary source term that fills in this depression. As the density profile flattens, diffusion transitions into a loss term and eventually dominates the depopulation process. As pressure increases, the occurrence of sign reversal in the diffusion term is delayed, and the magnitude of diffusion source is reduced.

Due to the rapid depletion of energetic electrons, the electron impact excitation rates drop sharply immediately after the power cut-off, causing the radiative source terms to vanish within a short time. When the pressure is raised, the higher collision frequency leads to enhanced electron impact rates, resulting in prolonged contribution from radiation and enlarged electron impact loss rates. Because both source and loss terms grow with increasing pressure, their relative variations determine the net decay behavior of the metastable population.

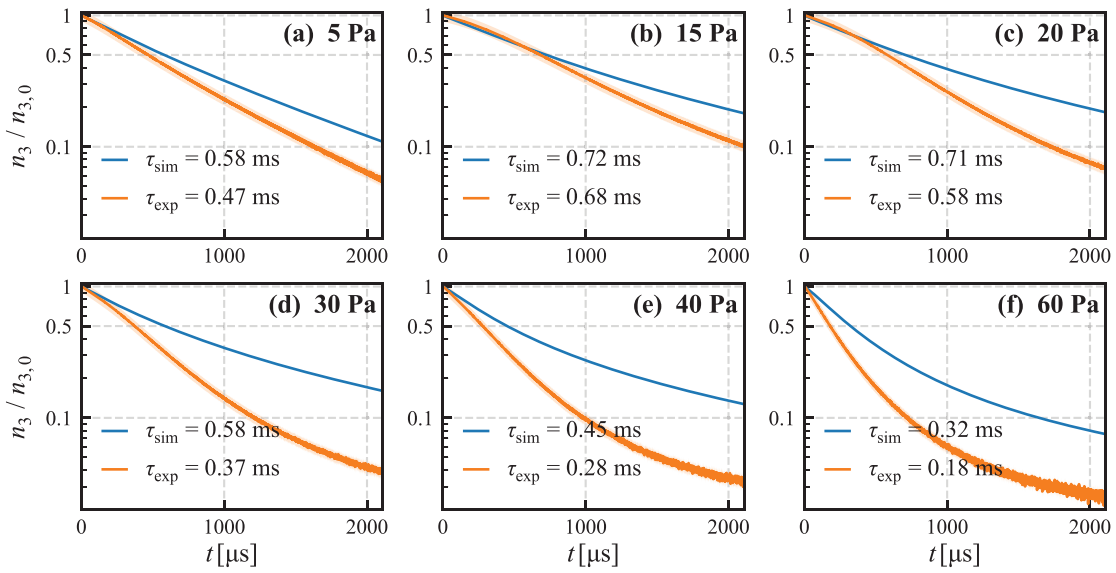



**Figure 10.** Temporal evolution of central Ar $1s_3$ density normalized by initial value $n_{3,0}$ under different pressures. The shaded areas represent the uncertainty in the experimental data.

As a general observation, one may note that cascade contributions from high-lying atomic energy levels to the population of the 1s levels disappear immediately after the termination of the RF excitation and that quenching and radial diffusion losses play minor roles in the balance of the $1s_5$ level.

The temporal decay of the other lower density metastable level, $1s_3$, is presented in figure 10. The decay rates obtained from simulations are lower than those from experiments, indicating smaller loss factors for metastable levels in the numerical model. The values, however, still agree within a factor of about four even during a long time period of 2000 $\mu$s. The larger deviation between experiment and simulation for the $1s_3$ level, compared with that for $1s_5$, may be attributed to the fact that rate data involving the latter have generally been more extensively benchmarked in previous experimental and theoretical studies, whereas some transfer or excitation channels of the $1s_3$ level remain less well constrained [31, 63].

In short terms, both metastable levels decay in a period lasting several milliseconds during the afterglow. The decay rates of atomic densities vary non-monotonically with increasing pressure, dominated by diffusion and electron impact processes.

### 5.2. 2p levels

Two representative higher excited levels, $2p_1$ and $2p_9$, are selected to illustrate their characteristic temporal behaviors, and the radiation emerging from these levels (with wavelengths 750.39 nm and 811.53 nm, respectively), during the afterglow. The time-resolved (experimental) emission intensities and the (computed) radiative emission rates from these levels are presented and compared in figure 11.

The experimental data show a rapid drop in emission intensity that occurs on the timescale of falling edge of the pulsed RF voltage, $\tau \approx 2\,\mu$s, for both transitions, which is followed by a slower decay with a characteristic decay time on the order of $\tau \approx 10\,\mu$s. The initial decay of the intensity is most pronounced for the transition originating from the $2p_1$ level ($\lambda = 750.39$ nm) at low pressure (see figure 11(a)). Under these conditions, the intensity falls below the detection limit within a few microseconds after the termination of RF power. For the same transition, at the higher pressure of 20 Pa, we observe an initial decay of an order of magnitude in the intensity, which is followed by a much slower decay over an extended timescale. At 60 Pa, the initial decay becomes even smaller. The characteristic decay times resulting from an exponential fitting to the data during the slower decay stage, are listed in table 2. The exponential fitting is applied to the period starting immediately after the termination of the RF excitation pulse and extending to the end of the measurement window, except for the 60 Pa case, where the fitting is restricted to $t < 15\,\mu$s.

For the other transition studied, $2p_9 \rightarrow 1s_5$ ($\lambda = 811.53$ nm), the two characteristic parts of the decay can also clearly be observed, but the initial decay is much less pronounced compared to the $2p_1 \rightarrow$

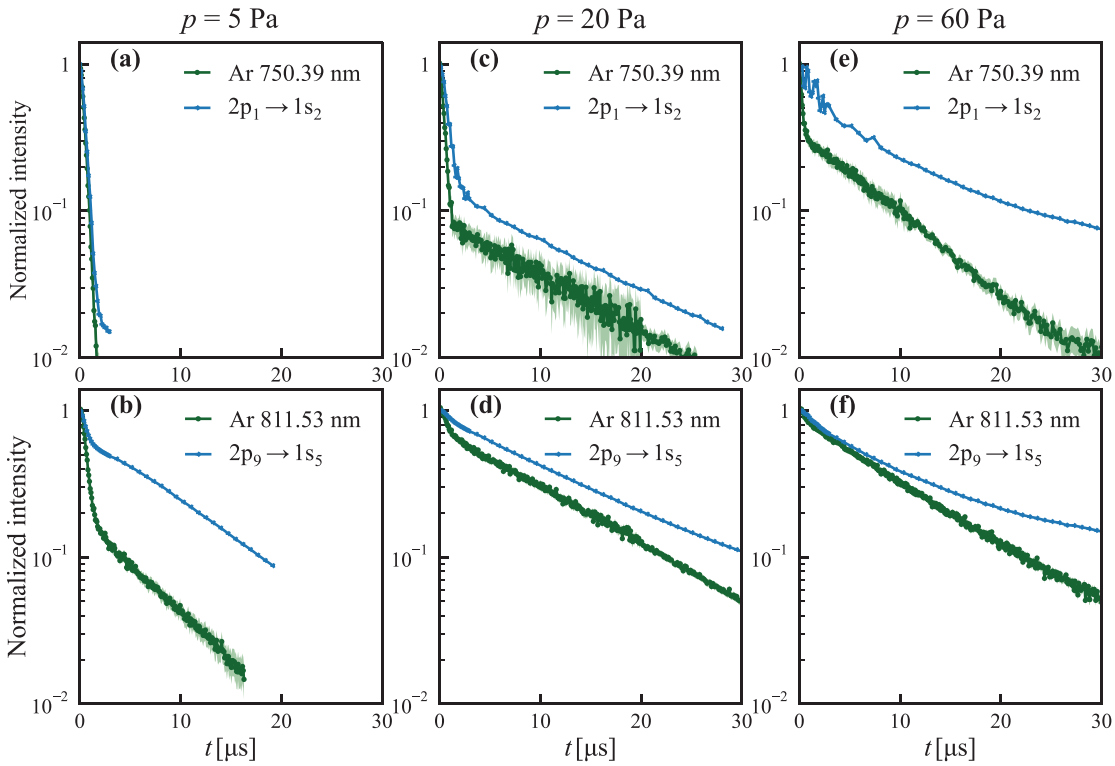



**Figure 11.** Measured and computed light emission at wavelength of 750.39 nm (top) and 811.53 nm (bottom) under different pressures. The intensities are normalized by the values at $t = 0$. The measured intensity spans up to two orders of magnitude. The shaded areas represent the uncertainty in the experimental data.

**Table 2.** Measured and computed exponential decay times of the $2p_9$ and $2p_1$ levels at different pressures.

| | $2p_1$ ($\mu$s) | | $2p_9$ ($\mu$s) | |
|---|---|---|---|---|
| Pressure (Pa) | Experiment | Simulation | Experiment | Simulation |
| 5 | | | 6.6 | 9.9 |
| 10 | | | 14.6 | 12.4 |
| 15 | | | 12.3 | 13.8 |
| 20 | 11.5 | 12.0 | 11.3 | 14.1 |
| 30 | 9.6 | 12.5 | 10.7 | 14.6 |
| 40 | 9.5 | 12.8 | 9.3 | 14.7 |
| 60 | 8.0 | 10.3 | 9.6 | 11.7 |

$1s_2$ transition discussed above. The long-time decay occurs on a similar time scale, as for the 750.39 nm line, as indicated by the data in table 2.

The differences in the magnitude of the initial decay originate from the different populating mechanisms of the two 2p levels considered. The 750.39 nm line can be efficiently populated from the Ar ground state by fast electrons. Therefore, its intensity is strongly affected by the disappearance of fast electrons in the early afterglow. The principal populating mechanism of the $2p_9$ level, radiating the 811.53 nm line, on the other hand, is known to be stepwise electron-impact excitation from the Ar $1s_5$ metastable level by lower-energy electrons, which are still present in the afterglow.

At later times, excitation from the ground state atoms is excluded and emission on both (and actually all) transitions originates exclusively from stepwise excitation from the 1s levels. The computational data for the radiative decay rates of the two 2p levels analyzed closely corroborate the existence of the two stages of the decay within the first few tens of microseconds, as seen in figure 11. The characteristic decay times in table 2 are also in fair agreement with those obtained from fitting to the experimental data, except for the $2p_1 \rightarrow 1s_2$ transition at the highest pressure, where the simulation predicts a higher emission intensity at later times, compared to the measured one.

The low light intensity in the afterglow does not make it possible to extend the measurements further in time, but the simulations allow computing the discharge characteristics over an extended

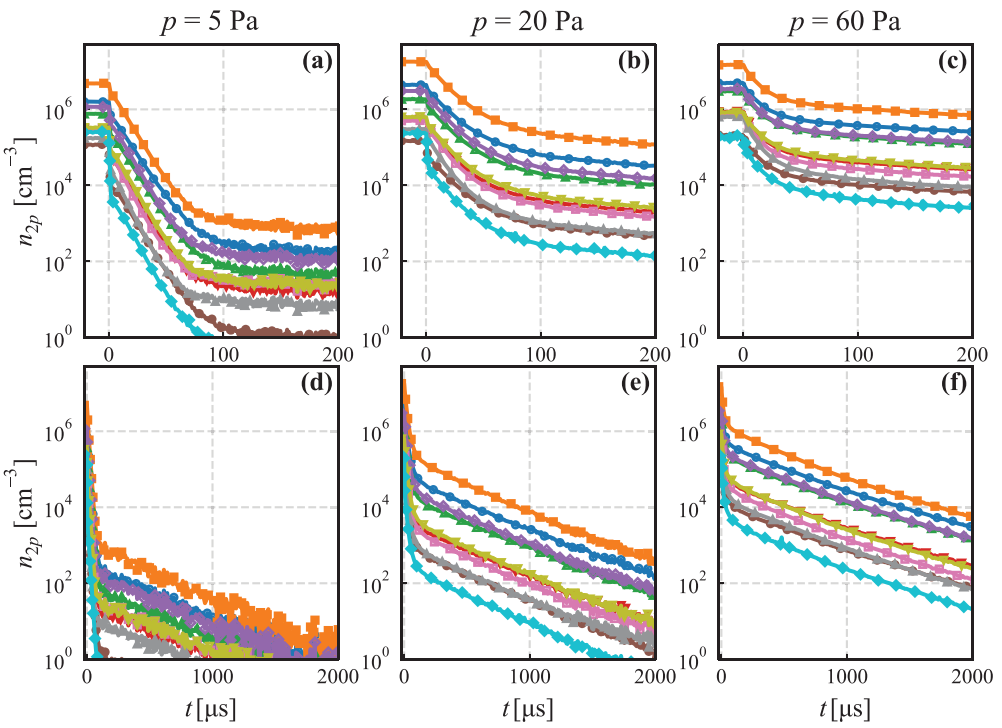



**Figure 12.** Computational results for the temporal evolution of central densities of Ar atoms in the 2p levels at different pressures. Panels in the second row present the same data over an extended time period.

timescale. The analysis of the decay of the 2p level densities, shown in figure 12, actually allows one to identify a third stage of the decay occurring over a time scale of hundreds of microseconds, significantly longer than the two time scales observable in figure 11. This third stage of decay is most obvious in the case of the lowest pressure (figure 12(a)), where we find a sharp transition between 50 $\mu$s and 100 $\mu$s. With increasing pressure, the transition becomes progressively softer and moves towards earlier times. Beyond these transitions the decay for all levels becomes extremely slow, similar to the decay of the 1s levels. This matching of the timescales is an indication for the coupling of the 1s and 2p levels by 'cyclic' repetition of stepwise excitation/radiation processes between these sets of levels. It should be noted that, at low densities, the computed populations of some 2p states exhibit increased numerical noise, which reduces the reliability of their absolute values in the late afterglow. However, the long-time behavior still qualitatively reflects the underlying physics.

Besides the decaying density of the 1s level populations, the changing electron density and EEPF have a further influence on the 2p level populations and the radiation emerging from these levels. Insights about these processes are provided by the simulations from which these characteristics are available: figure 13 shows the electron density, figure 14 the EEPF, while figures 15 and 16 the source and loss terms for the $2p_1$ and $2p_9$ levels. The electron density (see figure 13) decays over a long time scale of milliseconds, due to the relatively low electron temperature in the afterglow (see figure 14) and the low ion mobility that, especially at higher pressures, leads to a low ambipolar diffusion coefficient that controls the loss of charged species. The EEPFs are shown in figure 14 for three representative moments: the quasi-steady active-glow period before power cut-off (panel (a)) and averaged over the 8–12 $\mu$s (panel (b)) and 150–154 $\mu$s (panel (c)) time interval after power cut-off. For the power-on stage, the well-known behavior of the EEPFs is recovered [17, 68]. Once the external power is switched off, the EEPFs above ~10 eV shrink rapidly, especially under the lowest pressure. The time interval 8–12 $\mu$s belongs to the time during which OES data are acquired, see figure 11. These data indicate the presence of electrons with a distribution close to Maxwell–Boltzmann distributions with electron temperatures around 1 eV. At a later moment, around 150 $\mu$s, as shown in figure 14(c), we observe a further cooling of the electrons and the development of a peak at energies around 7.3 eV which is caused by the pooling ionization process. This process is the most important one, maintaining ionization in the afterglow (as will be confirmed later in the analysis of the various ionization processes). Less significant features above 10 eV originate from stepwise ionization.

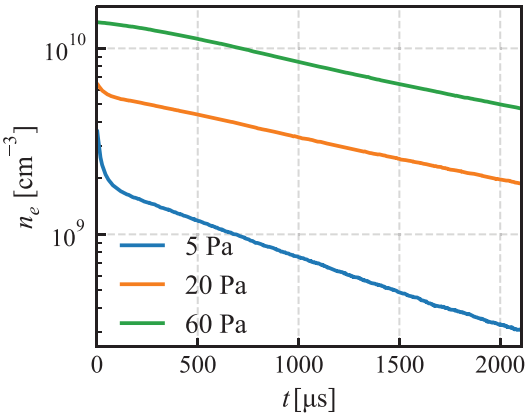



**Figure 13.** Simulation results for the temporal evolution of central electron density under different pressures.

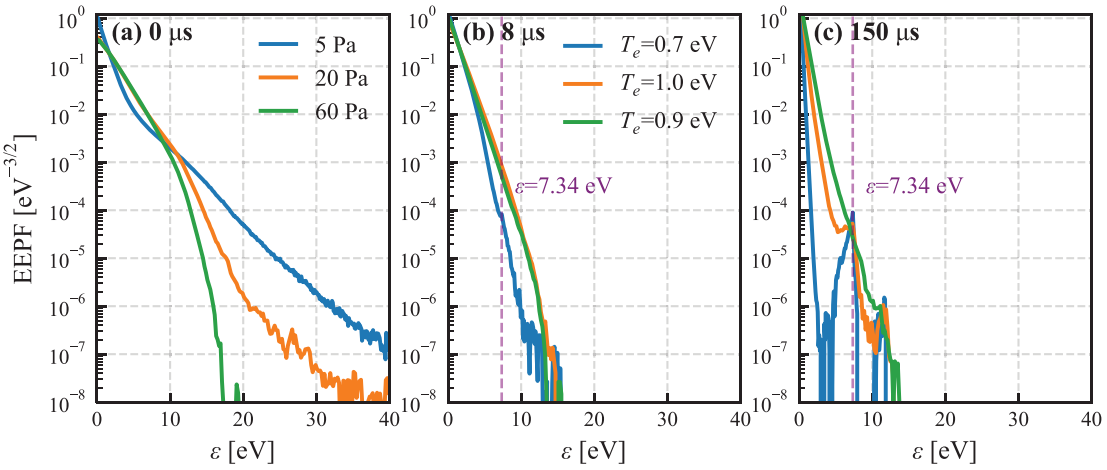



**Figure 14.** Calculated normalized EEPF in the center at quasi-steady active-glow (a), 8–12 $\mu$s (b) and 150–154 $\mu$s in the afterglow under different pressures. The legend in (b) shows the electron temperature obtained from a linear fit to the EEPF graphs in the energy range of 2–10 eV. The vertical dashed lines at 7.34 eV correspond to the energy of the electrons originating from the pooling process between two Ar 1s atoms.

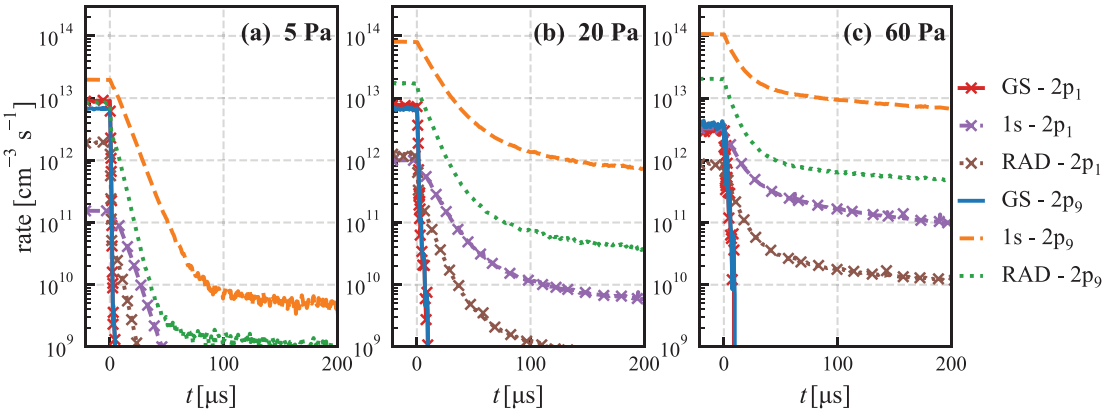



**Figure 15.** Temporal evolution of population rates for 2p levels under (a) 5 Pa, (b) 20 Pa, and (c) 60 Pa. The line style represents specific source from GS atoms (GS), 1s level (1s) or higher excited levels (RAD). The marker refers to 2p$_1$ level.

The analysis of the population rates of the 2p$_1$ and 2p$_9$ levels in figure 15 confirms the dominance of excitation from GS atoms for the former level and the dominance of stepwise excitation for the latter level, during the active discharge. While excitation from the ground state cuts off immediately after the termination of the RF power, stepwise excitation and radiation from higher levels are confirmed

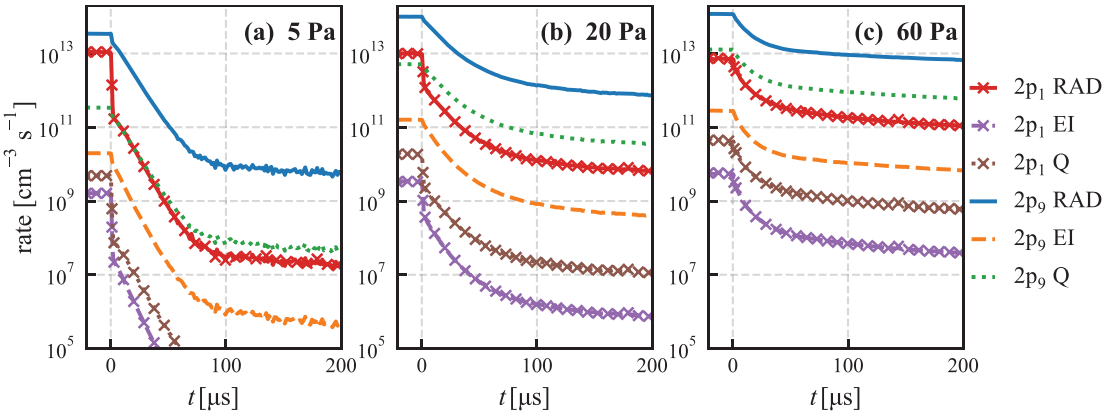



**Figure 16.** Temporal evolution of depopulation rates for 2p levels under (a) 5 Pa, (b) 20 Pa, and (c) 60 Pa. The line style represents specific loss by radiation (RAD), electron impact (EI) and quenching by GS atoms (Q).

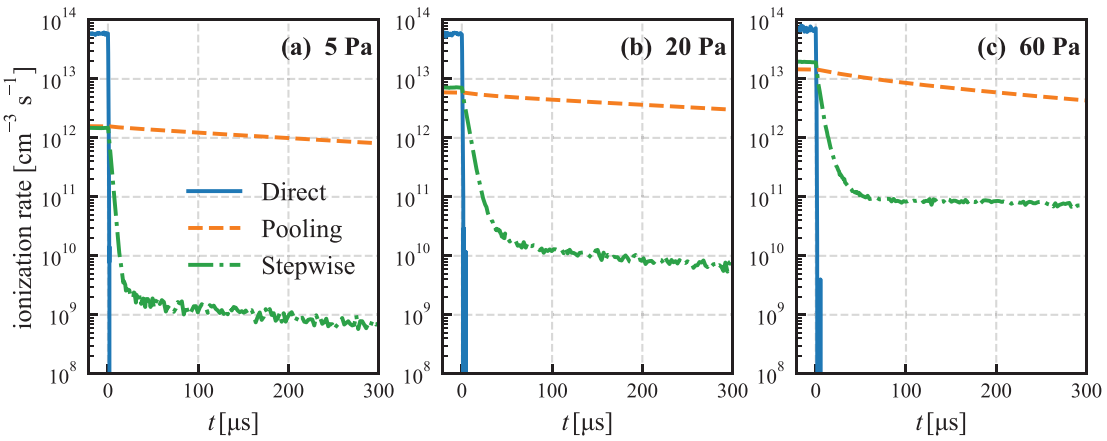



**Figure 17.** Simulation results for the temporal evolution of spatially averaged ionization rates under different pressures.

to remain the populating mechanisms for both 2p levels. Both of these sources exhibit a characteristic change with time for both levels. A change in the slope of the graphs is most obvious in the case of the lowest pressure, where we find a sharp transition between 50 $\mu$s and 100 $\mu$s, explaining the observations made in figure 12. With increasing pressure the transition becomes progressively softer and moves towards earlier times. Similar temporal characteristics of the loss rates due to various mechanisms of the 2p levels can be identified in figure 16. For both levels, radiation represents the dominant loss, which is followed by quenching and electron-impact collisions.

### 5.3. Ionization process

Finally, we assess the role of excited species in ionization in the afterglow. It is well established that metastable atoms can make a significant contribution to ionization in quasi-steady discharges, owing to their relatively high population densities and lower ionization energy thresholds compared with GS atoms [69]. Metastable species also play a crucial role during the afterglow period, when the external power supply is switched off. As a result of the rapid loss of energetic electrons, the direct ionization rate via GS atoms decreases sharply, as illustrated in figure 17, which shows the spatially averaged rates of the various ionization channels in quasi-steady discharge ($t < 0$) and afterglow ($t > 0$). The stepwise ionization process decays slightly slower than the direct ionization; however, since both processes rely on electron impact, their contributions become negligible within approximately 50 $\mu$s. In contrast, ionization induced by pooling reactions between 1s levels exhibits a much slower decay and therefore dominates the ionization mechanisms during the late afterglow phase.

Gas pressure has a pronounced influence on the relative contribution of different ionization pathways. During the active-glow phase, direct ionization remains the dominant mechanism at all investigated pressures. Nevertheless, the absolute rates of both stepwise and pooling ionization increase with

increasing pressure, reflecting the enhanced population of metastable levels under higher collision frequency. This pressure-induced promotion of indirect ionization channels persists into the afterglow. These results indicate that excited atoms play a crucial role in sustaining discharge ionization during both the active-glow and afterglow phases, and that their importance is significantly amplified with increasing gas pressure.

To some extent, the indirect ionization contributes to the electron density and energy in the afterglow period, as evidenced by the temporal evolution of electron density at the center of the discharge chamber shown in figure 13.

## 6. Conclusions

In the present work, the temporal evolution of Ar excited level populations was investigated by means of measurements and simulations. For experiments, time-resolved laser absorption spectroscopy was employed for the measurements of the densities of Ar $1s_5$ and $1s_3$ metastable species, while OES was used for acquiring emission from two of the Ar-I 2p levels. In numerical simulations, a combination of PIC/MCC module along with DRR module was used to obtain the spatio-temporally resolved densities of Ar excited levels and other discharge characteristics, like the rates of different ionization pathways.

The measured and computed absolute densities of the $1s_5$ and $1s_3$ metastable atoms in the quasi-steady discharge showed good agreement, which served as a validation of the discharge model, which was also applicable in the afterglow. The temporal decay rates of the metastable atoms, obtained experimentally and in the simulations showed a good agreement too, for the $1s_5$ atoms, while more significant deviations were seen for the $1s_3$ level.

The spatio-temporal distributions of the metastable atoms showed a pressure-dependent behavior. At the lowest pressure considered of 5 Pa, density peak was found in the center of the electrode gap both for the quasi-steady discharge and the afterglow. At higher pressures, the initial density distribution has a double-peaked structure because creation of the excited atoms tends to concentrate to regions around the sheath edges under such conditions. At intermediate pressures (e.g. at 20 Pa) this double-peaked structure changed to a central-peaked distribution in the afterglow, over a time period of about one millisecond. At the highest pressure considered, the double-peaked distribution was retained, due to the reduced rate of diffusion. The time and space-dependent analyses of the rates of the dominant populating and de-populating reactions allowed the explanation of these observations.

The populations of the Ar atoms in the 2p levels were found to decay rapidly in the afterglow at low pressure, the decay was, however, found to slow down as the pressure was increased. This behavior was caused by the stepwise excitation from long-lived 1s levels to the 2p levels, which created a coupling between the decays of these groups of levels. The experimental and computational results were found to be in reasonable agreement also for the dynamics of the 2p levels.

The analysis of the rates of various ionization processes in the afterglow showed (i) a rapid decay of the electron-impact ionization of ground state atoms, due to the rapid disappearance of fast electrons, (ii) a relatively fast decay of the stepwise ionization processes as these also require electrons with several eV-s, and (iii) consequently, a prominence of the pooling ionization by collisions of Ar 1s atoms, which have a long lifetime, extending several milliseconds. This latter process is thus essential for the maintenance of the plasma for several milliseconds in the late afterglow.

## Data availability statement

The data that support the findings of this study are available upon reasonable request from the authors.

## ORCID iDs

Lan-Yue Luo 0009-0009-8522-8664
Zoltán Donkó 0000-0003-1369-6150
Ranna Masheyeva 0000-0002-6950-662X
He-Ping Li 0000-0002-3149-757X
Peter Hartmann 0000-0003-3572-1310

## References


[1] Makabe T and Petrovic Z L 2006 *Plasma Electronics: Applications in Microelectronic Device Fabrication* (CRC Press)
[2] Truica-Marasescu F and Wertheimer M R 2008 *Plasma Process. Polym.* **5** 44–57
[3] Ouyang B, Zhang Y, Wang Y, Zhang Z, Fan H J and Rawat R S 2016 *J. Mater. Chem. A* **4** 17801–8
[4] Sekine M 2002 *Appl. Surf. Sci.* **192** 270–98
[5] Donkó Z, Schulze J, Czarnetzki U, Derzsi A, Hartmann P, Korolov I and Schüngel E 2012 *Plasma Phys. Control. Fusion* **54** 124003
[6] Goto H H, Lowe H D and Ohmi T 1993 *IEEE Trans. Semicond. Manuf.* **6** 58–64
[7] Georgieva V and Bogaerts A 2005 *J. Appl. Phys.* **98** 023308
[8] Booth J P, Curley G, Marić D and Chabert P 2009 *Plasma Sources Sci. Technol.* **19** 015005
[9] Hartmann P, Korolov I, Escandón-López J, Van Gennip W, Buskes K and Schulze J 2022 *Plasma Sources Sci. Technol.* **31** 055017
[10] Schmidt F, Schulze J, Johnson E, Booth J P, Keil D, French D M, Trieschmann J and Mussenbrock T 2018 *Plasma Sources Sci. Technol.* **27** 095012
[11] Economou D J 2014 *J. Phys. D: Appl. Phys.* **47** 303001
[12] Maeshige K, Washio G, Yagisawa T and Makabe T 2002 *J. Appl. Phys.* **91** 9494–501
[13] Ohmori T, Goto T, Kitajima T and Makabe T 2003 *Appl. Phys. Lett.* **83** 4637–9
[14] Chaubey N and Goree J 2023 *J. Appl. Phys.* **56** 375202
[15] Agarwal A, Rauf S and Collins K 2011 *Appl. Phys. Lett.* **99** 021501
[16] Wen D Q, Krek J, Gudmundsson J T, Kawamura E, Lieberman M A and Verboncoeur J P 2021 *Plasma Sources Sci. Technol.* **30** 105009
[17] Donkó Z, Hartmann P, Korolov I, Schulenberg D, Rohr S, Rauf S and Schulze J 2023 *Plasma Sources Sci. Technol.* **32** 065002
[18] Liu R, Liu Y, Jia W and Zhou Y 2017 *Phys. Plasmas* **24** 013517
[19] Overzet L J and Kleber J 1998 *Plasma Sources Sci. Technol.* **7** 512
[20] Wenig G, Schulze M, Awakowicz P and v Keudell A 2006 *Plasma Sources Sci. Technol.* **15** S35
[21] Proshina O, Rakhimova T, Kovalev A, Vasilieva A, Zotovich A, Zyryanov S and Rakhimov A 2020 *Plasma Sources Sci. Technol.* **29** 015015
[22] Kovalev A, Rakhimova T, Rakhimov A, Proshina O, Vasilieva A and Voloshin D 2021 *Phys. Plasmas* **28** 093507
[23] Biondi M A 1954 *Phys. Rev.* **93** 1136
[24] Demidov V, De Joseph J C and Kudryavtsev A 2005 *Phys. Rev. Lett.* **95** 215002
[25] Gorchakov S, Loffhagen D and Uhrlandt D 2006 *Phys. Rev. E* **74** 066401
[26] Celik Y, Tsankov T V, Aramaki M, Yoshimura S, Luggenhölscher D and Czarnetzki U 2012 *Phys. Rev. E* **85** 056401
[27] Tsankov T V, Johnsen R and Czarnetzki U 2015 *Plasma Sources Sci. Technol.* **24** 065001
[28] An R, Li Z, Jiang C, Xia C, He L, Yang S, Wu H and Jiang W 2025 *Plasma Sources Sci. Technol.* **34** 115001
[29] Boffard J B, Piech G A, Gehrke M F, Anderson L and Lin C C 1999 *Phys. Rev. A* **59** 2749
[30] Zhu X M, Cheng Z W, Carbone E, Pu Y K and Czarnetzki U 2016 *Plasma Sources Sci. Technol.* **25** 043003
[31] Cheng Z W, Zhu X M, Liu F X and Pu Y K 2014 *J. Phys. D: Appl. Phys.* **47** 275203
[32] Boffard J B, Wang S, Lin C C and Wendt A 2015 *Plasma Sources Sci. Technol.* **24** 065005
[33] Denysenko I, Stefanović I, Sikimić B, Winter J, Azarenkov N and Sadeghi N 2011 *J. Phys. D: Appl. Phys.* **44** 205204
[34] Kang N, Gaboriau F, Oh S G and Ricard A 2011 *Plasma Sources Sci. Technol.* **20** 035002
[35] Luo L Y, Donkó Z, Masheyeva R, Vass M, Li H P and Hartmann P 2025 *Plasma Sources Sci. Technol.* **34** 015009
[36] Zatsarinny O, Wang Y and Bartschat K 2014 *Phys. Rev. A* **89** 022706
[37] Iordanova S and Koleva I 2007 *Spectrochim. Acta B.* **62** 344–56
[38] Derzsi A, Hartmann P, Vass M, Horváth B, Gyulai M, Korolov I, Schulze J and Donkó Z 2022 *Plasma Sources Sci. Technol.* **31** 085009
[39] Derzsi A, Vass M, Masheyeva R, Horvath B, Donko Z and Hartmann P 2024 *Plasma Sources Sci. Technol.* **33** 025005
[40] Vass M, Wilczek S, Lafleur T, Brinkmann R P, Donkó Z and Schulze J 2021 *Plasma Sources Sci. Technol.* **30** 065015
[41] Schulenberg D A, Korolov I, Donkó Z, Derzsi A and Schulze J 2021 *Plasma Sources Sci. Technol.* **30** 105003
[42] BSR database (available at: www.lxcat.net) (Accessed 18 August 2022)
[43] Zatsarinny O and Bartschat K 2013 *J. Phys. B: At. Mol. Opt. Phys.* **46** 112001
[44] Pitchford L C *et al* 2017 *Plasma Process. Polym.* **14** 1600098
[45] Carbone E, Graef W, Hagelaar G, Boer D, Hopkins M M, Stephens J C, Yee B T, Pancheshnyi S, van Dijk J and Pitchford L 2021 *Atoms* **9** 16
[46] Gangwar R, Sharma L, Srivastava R and Stauffer A 2012 *J. Appl. Phys.* **111** 053307
[47] Hyman H 1979 *Phys. Rev. A* **20** 855
[48] Lymberopoulos D P and Economou D J 1993 *J. Appl. Phys.* **73** 3668–79
[49] Phelps A V 1994 *J. Appl. Phys.* **76** 747–53
[50] Turner M M 2006 *Phys. Plasmas* **13** 033506
[51] Vass M, Palla P and Hartmann P 2022 *Plasma Sources Sci. Technol.* **31** 064001
[52] Welch D R, Genoni T C, Clark R E and Rose D V 2007 *J. Comput. Phys.* **227** 143–55
[53] Chang R and Setser D 1978 *J. Chem. Phys.* **69** 3885–97
[54] Sadeghi N, Setser D, Francis A, Czarnetzki U and Döbele H 2001 *J. Chem. Phys.* **115** 3144–54
[55] Ellis E and Twiddy N 1969 *J. Phys. B: At. Mol. Phys.* **2** 1366
[56] Tachibana K 1986 *Phys. Rev. A* **34** 1007
[57] LeVeque R J 2007 Finite difference methods for ordinary and partial differential equations: steady-state and time-dependent problems (Society for Industrial and Applied Mathematics)
[58] Siepa S L 2017 Global collisional-radiative model for optical emission spectroscopy of argon and argon-containing plasmas *PhD Thesis Dissertation*, Bochum, Ruhr-Universität Bochum
[59] Bhatia A and Kastner S 2000 *J. Quant. Spectrosc. Radiat. Transfer* **67** 55–63
[60] Capriotti E R 1965 *Astrophys. J.* **142** 1101
[61] Zhang X, Wang X K, Lin Z R, Zhao K and Liu Y X 2026 *J. Phys. D: Appl. Phys.* **59** 035205
[62] Stankov M, Becker M M, Hoder T and Loffhagen D 2022 *Plasma Sources Sci. Technol.* **31** 125002
[63] Carbone E, Van Veldhuizen E, Kroesen G and Sadeghi N 2015 *J. Phys. D: Appl. Phys.* **48** 425201
[64] McMillin B K and Zachariah M R 1995 *J. Appl. Phys.* **77** 5538–44

[65] Ohba T and Makabe T 2010 *Appl. Phys. Lett.* **96** 111501
[66] Lauro-Taroni L, Turner M and Braithwaite N S 2004 *J. Phys. D: Appl. Phys.* **37** 2216
[67] Kramida A, Ralchenko Y, Reader J and Team N A 2024 NIST atomic spectra database (version 5.12) (available at: https://doi.org/10.18434/T4W30F)
[68] Godyak V, Piejak R and Alexandrovich B 1992 *Plasma Sources Sci. Technol.* **1** 36–58
[69] Ferreira C, Loureiro J and Ricard A 1985 *J. Appl. Phys.* **57** 82–90